



Selective catalytic reduction of NO_x by NH_3 over CeO_2 supported on TiO_2 : Comparison of anatase, brookite, and rutile

Xiaojiang Yao ^{a,b,*}, Ruidun Zhao ^c, Li Chen ^a, Jun Du ^c, Changyuan Tao ^c, Fumo Yang ^{a,b,*}, Lin Dong ^d

^a Research Center for Atmospheric Environment, Chongqing Institute of Green and Intelligent Technology, Chinese Academy of Sciences, Chongqing 400714, PR China

^b Center for Excellence in Regional Atmospheric Environment, Institute of Urban Environment, Chinese Academy of Sciences, Xiamen 361021, PR China

^c School of Chemistry and Chemical Engineering, Chongqing University, Chongqing 400044, PR China

^d Jiangsu Key Laboratory of Vehicle Emissions Control, Center of Modern Analysis, Nanjing University, Nanjing 210093, PR China

ARTICLE INFO

Article history:

Received 24 November 2016

Received in revised form 9 February 2017

Accepted 18 February 2017

Available online 21 February 2017

Keywords:

Ceria-based catalysts

TiO_2

Crystal form

Interaction

$\text{NH}_3\text{-SCR}$ reaction

ABSTRACT

Anatase (A) TiO_2 is widely used as a support of the supported vanadium-based and non-vanadium-based catalysts for $\text{NH}_3\text{-SCR}$ reaction. However, there is lack of enough attention for brookite (B) and rutile (R) TiO_2 . Therefore, in the present work, we synthesize a series of $\text{TiO}_2\text{-A}$, $\text{TiO}_2\text{-B}$, and $\text{TiO}_2\text{-R}$, and then used as supports to prepare $\text{CeO}_2/\text{TiO}_2\text{-A}$, $\text{CeO}_2/\text{TiO}_2\text{-B}$, and $\text{CeO}_2/\text{TiO}_2\text{-R}$ catalysts with the purpose of clarifying the crystal form effect of TiO_2 supports on the physicochemical properties and catalytic performance of these supported ceria-based catalysts for $\text{NH}_3\text{-SCR}$ reaction. Characterization results exhibit that H_2 consumption (responding to reduction property), acid amounts, surface Ce^{3+} content, surface adsorbed oxygen species, and catalytic performance of these supported ceria-based catalysts give the order of $\text{CeO}_2/\text{TiO}_2\text{-R} > \text{CeO}_2/\text{TiO}_2\text{-B} > \text{CeO}_2/\text{TiO}_2\text{-A}$, which is related to the interaction (*i.e.*, $\text{Ce}^{3+} + \text{Ti}^{4+} \leftrightarrow \text{Ce}^{4+} + \text{Ti}^{3+}$) between CeO_2 and TiO_2 (anatase, brookite, and rutile). Especially, $\text{CeO}_2/\text{TiO}_2\text{-R}$ catalyst exhibits the optimal catalytic performance for $\text{NH}_3\text{-SCR}$ reaction among these supported ceria-based catalysts owing to the most excellent reduction property as well as the largest amounts of acid sites, surface Ce^{3+} content, and surface adsorbed oxygen species.

© 2017 Elsevier B.V. All rights reserved.

1. Introduction

$\text{V}_2\text{O}_5\text{-WO}_3/\text{TiO}_2$ and $\text{V}_2\text{O}_5\text{-MoO}_3/\text{TiO}_2$ catalysts are practically applied for the selective catalytic reduction of nitrogen oxides (NO_x) by NH_3 ($\text{NH}_3\text{-SCR}$) to control the emission of NO_x from stationary sources (such as coal-fired power plants), which is because of their good catalytic performance and excellent resistance to SO_2 [1–5]. As early as 1994, Topsøe et al. [6] pointed out that the catalytic cycle of $\text{NH}_3\text{-SCR}$ consists redox and acid cycles over vanadium-based catalysts based on transient or steady-state *in situ* Fourier transform infrared spectroscopy (FTIR) experiments. In addition, it is well known that with regard to $\text{V}_2\text{O}_5\text{-WO}_3/\text{TiO}_2$ and $\text{V}_2\text{O}_5\text{-MoO}_3/\text{TiO}_2$ catalysts, V_2O_5 is the main redox active site, WO_3 (or MoO_3) provides surface acidity, and TiO_2 is used as a support

with superior resistance to SO_2 [1,7]. However, there are some disadvantages in this kind of catalysts, such as the biological toxicity of V_2O_5 , narrow operating temperature window, generation of large amount of N_2O at high temperature, and high activity for the oxidation of SO_2 to SO_3 , etc. [8–10]. Therefore, it is very significant to develop a novel environment-friendly non-vanadium-based catalyst with excellent catalytic performance and high resistance to SO_2 for $\text{NH}_3\text{-SCR}$.

In recent years, ceria (CeO_2) has been widely investigated in $\text{NH}_3\text{-SCR}$ reaction due to its good redox property and high storage/release oxygen capacity, associated with the abundant oxygen vacancy and facile shift of $\text{Ce}^{3+}/\text{Ce}^{4+}$ [11–13]. Pure CeO_2 exhibits poor $\text{NH}_3\text{-SCR}$ reactivity, but its catalytic performance can be remarkably enhanced by the following two approaches [14–17]: (1) combining with other metal-oxides to synthesize ceria-based mixed-oxide catalysts; and (2) highly dispersed on the surface of supports to prepare supported ceria-based catalysts. For example, He et al. [15] synthesized a $\text{CeO}_2\text{-TiO}_2$ mixed-oxide catalyst through an optimized homogeneous precipitation method, and found that its catalytic performance is better than that of $\text{V}_2\text{O}_5\text{-WO}_3/\text{TiO}_2$

* Corresponding authors at: Chongqing Institute of Green and Intelligent Technology, Chinese Academy of Sciences, Fangzheng Avenue 266#, Chongqing 400714, PR China. Tel.: +86 23 65935909; fax: +86 23 65935924.

E-mail addresses: yaoxj@cigit.ac.cn (X. Yao), fmyang@cigit.ac.cn (F. Yang).

catalyst for NH₃-SCR due to the synergistic effect between CeO₂ and TiO₂. Li et al. [10] reported that CeO₂/TiO₂-SiO₂ catalysts prepared by a wet impregnation method exhibited excellent NH₃-SCR reactivity, high N₂ selectivity, and good resistance to SO₂ and H₂O, which is attributed to the highly dispersion of CeO₂ on the surface of TiO₂-SiO₂ support, the conversion of Ce⁴⁺ to Ce³⁺, and the increase of Brønsted (B) acid sites.

As mentioned above, TiO₂ has superior resistance to SO₂, so it is widely used as a support of non-vanadium-based catalysts for NH₃-SCR [18–20]. It is well known that TiO₂ consists three crystal forms of anatase, brookite, and rutile. In the past years, the crystal form effect of TiO₂ on the catalytic performance of titanium-based catalysts has been deeply discussed for some photocatalytic reactions, such as photocatalytic reduction of CO₂, photocatalytic oxygen evolution, photocatalytic hydrogen production, and photocatalytic degradation of water pollutants, etc. [21–27]. As we all know that anatase usually exhibits better photocatalytic activity than that of brookite and rutile. Nevertheless, there are numerous examples for the unexpectedly high activity of brookite and rutile. For example, Li et al. [28] prepared a series of anatase, brookite, and rutile TiO₂ catalysts for photocatalytic reduction of CO₂, and found that helium (He) pretreatment of these catalysts at a moderate temperature led to the generation of oxygen vacancy and Ti³⁺ on the surface of anatase and brookite except rutile. Furthermore, they pointed out that the photocatalytic performance of defective brookite is better than that of anatase and rutile due to the lowest formation energy of oxygen vacancy on the surface of brookite. Macyk et al. [29] compared the photocatalytic performance of anatase and rutile TiO₂ for oxygen activation, and reported that rutile is a good photocatalyst for the activation of molecular oxygen because that more efficient O₂^{•-} production happens on the surface of rutile, which is related to the good adsorption of oxygen and the low redox potential of the excited electron. However, the crystal form effect of TiO₂ on the catalytic performance of the supported non-vanadium-based catalysts for NH₃-SCR has not yet been reported. In view of the successful application of anatase TiO₂ in V₂O₅-WO₃/TiO₂ and V₂O₅-MoO₃/TiO₂ catalysts for NH₃-SCR, the current investigation of TiO₂ supports for the supported non-vanadium-based denitration catalysts is mainly focused on anatase. Therefore, it is necessary to carry out a comparative research about anatase, brookite, and rutile supporting non-vanadium-based denitration catalysts.

In the present work, we synthesized a series of anatase, brookite, and rutile TiO₂, and then used as supports to prepare the supported ceria-based catalysts for NH₃-SCR. The obtained samples were characterized by means of XRD, Raman, N₂-physisorption, H₂-TPR, NH₃-TPD, *in situ* DRIFTS, XPS, and NH₃-SCR model reaction with the purpose of exploring the crystal form effect of TiO₂ on the physicochemical properties and catalytic performance of CeO₂/TiO₂ catalysts for NH₃-SCR.

2. Experimental section

2.1. Catalysts preparation

Three crystal forms of TiO₂ were respectively prepared by precipitation, hydrothermal treatment, and sol-gel methods according to the literatures [13,28]. To prepare anatase TiO₂, the required amount of TiCl₄ was dissolved in distilled water (containing 1% v/v concentrated HCl) with magnetic stirring during an ice-water bath. And then, ammonia (25%) was dropwisely added into the above TiCl₄ solution with magnetic stirring until pH = 10. The resulting suspension was kept in stirring for another 3 h, aged 24 h, and subsequently filtered, washed several times with distilled water until pH = 7 and no Cl⁻ detected by AgNO₃. For brookite TiO₂, the desired amount of titanium(IV) bis(ammonium lactato) dihydroxide (TALH,

C₆H₁₈N₂O₈Ti) aqueous solution (50%) and a quantitative amount of 7 M urea were dissolved in distilled water and mixed together with magnetic stirring for 1 h. The resulting solution was transferred into a Teflon-lined autoclave, and then heated from room temperature to 160 °C and held for 24 h in an oven. After that, the autoclave was naturally cooled to room temperature in static air. The precipitate was filtered and washed several times with distilled water until pH = 7. With regard to rutile TiO₂, the desired amount of TiCl₄ was dropwisely added into the absolute ethanol with magnetic stirring for 1 h to form a transparent yellowish sol. And then, the obtained sol was slowly added into distilled water with magnetic stirring for another 1 h. In which, the molar ratio of TiCl₄, absolute ethanol, and distilled water was fixed at 1:10:140. After that, the solution was kept in a closed system at 50 °C for 24 h in an oven to obtain a yellowish gel. The resulting gel was naturally cooled to room temperature in static air, and then filtered, washed several times with distilled water until pH = 7 and no Cl⁻ detected by AgNO₃. Finally, all of these obtained cakes were oven dried at 110 °C overnight and subsequently calcined at 400 °C in the flowing air for 5 h. The prepared anatase, brookite, and rutile TiO₂ samples were denoted as TiO₂-A, TiO₂-B, and TiO₂-R, respectively.

The supported ceria-based catalysts were prepared by incipient-wetness impregnating the TiO₂-A, TiO₂-B, and TiO₂-R supports with Ce(NO₃)₃ solution. The mixture was kept in magnetic stirring for 1 h and evaporated to remove water at 110 °C during an oil bath. The obtained samples were oven dried at 110 °C overnight, and finally calcined at 400 °C for 5 h in the flowing air. Furthermore, the loading amount of CeO₂ was fixed at 0.4 mmol CeO₂/g-support. The prepared catalysts were denoted as CeO₂/TiO₂-A, CeO₂/TiO₂-B, and CeO₂/TiO₂-R, respectively.

2.2. Catalysts characterization

X-ray diffraction (XRD) patterns of these samples were recorded on a Philips X'Pert3 Powder diffractometer using Ni-filtered Cu K α radiation ($\lambda = 0.15418\text{ nm}$). The operating voltage and current of X-ray tube were fixed at 40 kV and 40 mA. The scan speed was set at $10^\circ \text{ min}^{-1}$ with a step size of 0.02° . The intensity data were collected from $2\theta = 10$ to 80° .

Raman spectra of these samples were collected on a Renishaw inVia Reflex Laser Raman spectrometer using Ar⁺ laser beam. The excitation wavelength was 532 nm and the laser power was 5 mW. The intensity data were collected from 100 to 1000 cm⁻¹.

Textural characteristics of these samples were obtained by N₂-physisorption at -196°C on a Belsorp-max analyzer, choosing Brunauer-Emmet-Teller (BET) method for calculating the specific surface area in the relative pressure range of $P/P_0 = 0\text{--}0.3$, and using Barrett-Joyner-Halenda (BJH) method for obtaining the pore distribution. Prior to each analysis, the sample was degassed under vacuum at 300 °C for 4 h.

H₂-temperature programmed reduction (H₂-TPR) experiments were performed in a quartz reactor connected to a thermal conductivity detector (TCD) with H₂-Ar mixture (7.0% H₂ by volume, 30 ml min⁻¹) as a reductant. Prior to the reduction, the catalyst (50 mg) was pretreated in high purified N₂ at 300 °C for 1 h, and then cooled to ambient temperature. After that, the H₂-TPR started from 100 to 900 °C at a rate of $10^\circ\text{C min}^{-1}$. The curve fitting was performed by using Origin 8.0 with a plugin of Peak Fitting Module (PFM). Furthermore, H₂ consumption of these samples was calibrated by CuO standard sample according to the calculation of peak area.

NH₃-temperature programmed desorption (NH₃-TPD) experiments were carried out on a dynamic chemisorption analyzer with a quartz reactor, detected by a thermal conductivity detector (TCD). About 200 mg catalyst was pretreated by high purified N₂ (30 ml min⁻¹) at 300 °C for 1 h. After pretreatment, the catalyst was

saturated with NH₃-N₂ mixture (1.0% NH₃ by volume, 30 ml min⁻¹) at 100 °C for 1 h and subsequently flushed with high purified N₂ (30 ml min⁻¹) at the same temperature for 1 h to remove the gaseous NH₃, and then cooled to ambient temperature. After that, the catalyst was heated from ambient temperature to 800 °C at a rate of 10 °C min⁻¹ in high purified N₂ (30 ml min⁻¹). The curve fitting was performed by using Origin 8.0 with a plugin of Peak Fitting Module (PFM).

In situ diffuse reflectance infrared Fourier transform spectra of NH₃-adsorption (NH₃-adsorption *in situ* DRIFTS) over these catalysts were collected on a Nicolet 5700 FT-IR spectrometer equipped with a high-sensitive MCT detector cooled by liquid N₂. The catalyst was placed in an *in situ* DRIFTS cell (Harrick) and pretreated by high purified N₂ at 450 °C for 1 h to remove the physisorbed water. The sample background of each target temperature was collected during the cooling process. At room temperature, the sample was exposed to NH₃-N₂ mixture (1.0% NH₃ by volume) at a rate of 50 ml min⁻¹ for 1 h to be saturated. And then, the gaseous NH₃ was purged by high purified N₂ (50 ml min⁻¹) for 1 h at the same temperature. *In situ* DRIFTS were recorded at various target temperatures from room temperature to 450 °C at a rate of 10 °C min⁻¹ in high purified N₂ by subtraction of the corresponding sample background.

X-ray photoelectron spectra (XPS) of these catalysts were performed on a PHI 5000 VersaProbe system, using monochromatic Al K α radiation (1486.6 eV) operating at an accelerating power of 15 kW. Before the measurement, the catalyst was outgassed at room temperature in a UHV chamber (<5 × 10⁻⁷ Pa). The sample charging effects were compensated by calibrating all binding energies (BE) with the adventitious C 1s peak at 284.6 eV. The curve fitting was performed by using XPSPEAK 4.1 with a Shirley-type background.

2.3. Catalytic performance measurement

The catalytic performance of these TiO₂ supports and supported ceria-based catalysts for NH₃-SCR model reaction was determined under steady state, involving a feed stream with a fixed composition of 500 ppm NO, 500 ppm NH₃, 5% O₂, 5% H₂O (when used), 100 ppm SO₂ (when used), and N₂ in balance. The catalyst (400 mg) was fitted in a quartz tube and pretreated with high purified N₂ at 300 °C for 1 h and then cooled to room temperature, after that, the mixed reaction gases were switched on. The reactions were carried out at different temperatures with a space velocity of 60000 ml g⁻¹ h⁻¹. NO and NO₂ concentrations of inlet and outlet were detected by a flue gas analyzer. N₂O concentration was measured by a N₂O analyzer. And NO_x conversion was calculated from the following equation:

$$\text{NO}_x \text{ conversion}(\%) = \frac{[\text{NO}]_{\text{in}} + [\text{NO}_2]_{\text{in}} - [\text{NO}]_{\text{out}} - [\text{NO}_2]_{\text{out}}}{[\text{NO}]_{\text{in}} + [\text{NO}_2]_{\text{in}}} \times 100\%$$

3. Results and discussion

3.1. Structural and textural characteristics (XRD, Raman, and N₂-physisorption)

The crystal form of TiO₂ and the dispersion state of CeO₂ are determined by XRD, and the corresponding results are displayed in Fig. 1. TiO₂-A exhibits a series diffraction peaks at 25.28, 36.95, 37.81, 38.58, 48.05, 54.04, 55.10, 62.69, 68.76, 70.31, and 75.13°, which are attributed to anatase [PDF-ICDD 21-1272]. TiO₂-B presents the characteristic peaks at 25.63, 30.87, 32.80, 36.33, 37.38, 40.20, 42.45, 46.16, 48.09, 49.25, 52.17, 54.32, 55.32, 57.25°, and so on, which are ascribed to brookite [PDF-ICDD 29-1360].

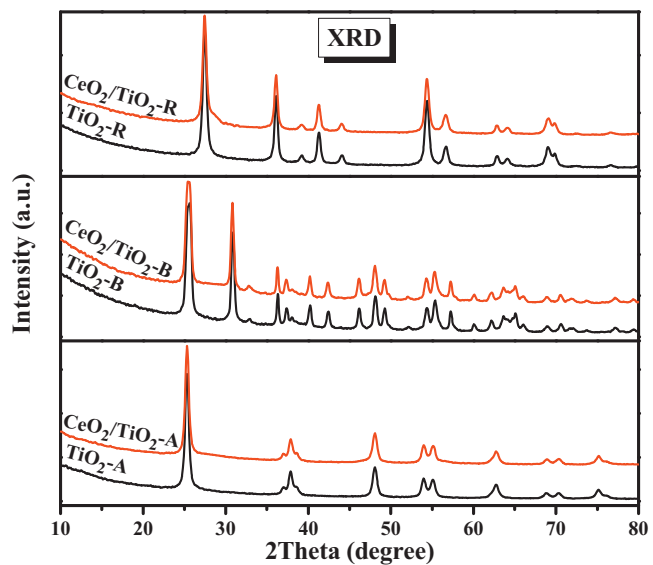


Fig. 1. XRD patterns of these supports and the corresponding supported ceria-based catalysts.

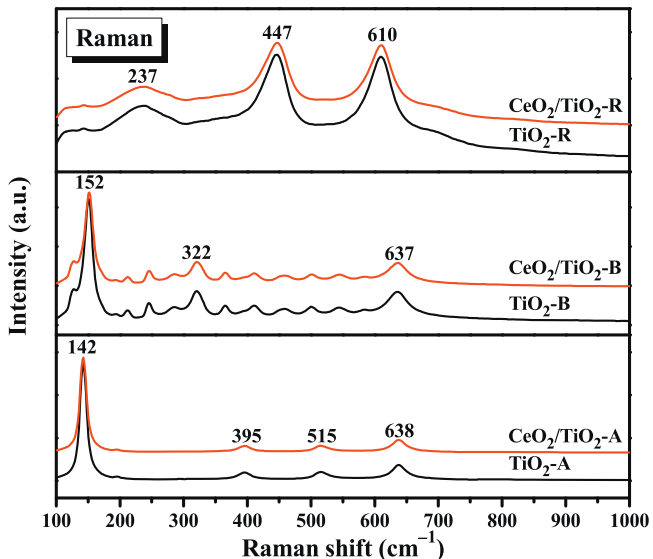


Fig. 2. Raman spectra of these supports and the corresponding supported ceria-based catalysts.

TiO₂-R displays its diffraction peaks at 27.45, 36.11, 39.20, 41.24, 44.06, 54.38, 56.64, 62.82, 64.04, 69.00, and 69.83°, which are assigned to rutile [PDF-ICDD 21-1276]. The obtained results indicate that three crystal forms of TiO₂ (i.e., anatase, brookite, and rutile) have been successfully synthesized in the present work. It can be seen from Fig. 1 that the XRD patterns of these supported ceria-based catalysts are very similar with the corresponding TiO₂ supports, and no diffraction peaks of CeO₂ [PDF-ICDD 34-0394] can be detected. Furthermore, we can find that the peak intensity of CeO₂/TiO₂-A, CeO₂/TiO₂-B, and CeO₂/TiO₂-R catalysts is weaker than that of the corresponding TiO₂ supports. These observations suggest that CeO₂ species is highly dispersed on the surface of TiO₂-A, TiO₂-B, and TiO₂-R supports [21,30].

Raman spectrum is chosen to further confirm the structure of these TiO₂ supports and supported ceria-based catalysts, as shown in Fig. 2. TiO₂-A gives four Raman bands at 142, 395, 515, and 638 cm⁻¹, which is consistent with the Raman spectrum of anatase [13,28]. TiO₂-B exhibits a series of complex Raman bands, which are

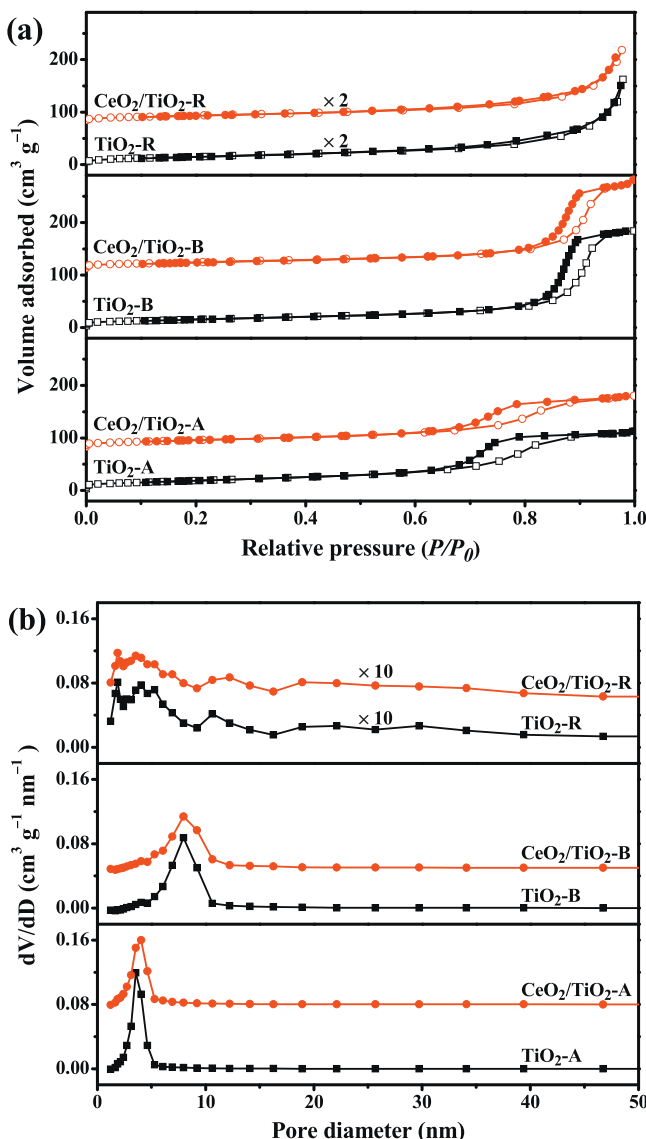


Fig. 3. (a) N₂ adsorption-desorption isotherms and (b) BJH pore distribution curves of these supports and the corresponding supported ceria-based catalysts.

related to brookite, and the strongest three Raman bands appear at 152, 322, and 637 cm⁻¹ [27,28]. TiO₂-R presents three Raman bands at 237, 447, and 610 cm⁻¹, which indicates a rutile structure [21,27]. These experimental results are in well agreement with XRD, and further confirm that we have successfully synthesized anatase, brookite, and rutile TiO₂ supports. Simultaneously, Raman spectra of these supported ceria-based catalysts are very similar with those of the corresponding TiO₂ supports, and F_{2g} Raman vibration mode of CeO₂ is absent. Moreover, the Raman band intensity of the catalysts is obviously weaker than that of supports, which suggests that the high dispersion of CeO₂ species on the surface of TiO₂-A, TiO₂-B, and TiO₂-R covers these supports and weakens the signals.

Fig. 3 displays N₂ adsorption-desorption isotherms and BJH pore distribution curves of these TiO₂ supports and the corresponding supported ceria-based catalysts. It can be seen from Fig. 3(a) that all of these samples exhibit the classical IV-type isotherm with an obvious type H1 (for TiO₂-A, TiO₂-B, CeO₂/TiO₂-A, and CeO₂/TiO₂-B) or H3 (for TiO₂-R and CeO₂/TiO₂-R) hysteresis loop as defined by IUPAC, which indicates that mesopore (2–50 nm) structure exists in these samples [19,21,31]. The mesopore structure of these

Table 1

BET specific surface area, total pore volume, and mean pore diameter of these supports and the corresponding supported ceria-based catalysts.

Samples	BET specific surface area (m ² g ⁻¹)	Total pore volume (cm ³ g ⁻¹)	Mean pore diameter (nm)
TiO ₂ -A	70.8	0.1871	10.6
TiO ₂ -B	57.6	0.2981	20.7
TiO ₂ -R	28.9	0.1257	17.4
CeO ₂ /TiO ₂ -A	59.6	0.1711	11.5
CeO ₂ /TiO ₂ -B	53.0	0.2623	19.8
CeO ₂ /TiO ₂ -R	25.7	0.1223	19.1

samples is formed by the agglomeration or compaction of particles [31]. Type H1 hysteresis loop of TiO₂-A, TiO₂-B, CeO₂/TiO₂-A, and CeO₂/TiO₂-B suggests their uniform and narrow distributions of pore size, while Type H3 hysteresis loop of TiO₂-R and CeO₂/TiO₂-R indicates their slit-shaped pores formed by the agglomeration of plate-like particles [31]. Indeed, Fig. 3(b) exhibits that the pore size distributions of TiO₂-A, TiO₂-B, CeO₂/TiO₂-A, and CeO₂/TiO₂-B are obviously better and narrower than those of TiO₂-R and CeO₂/TiO₂-R, while all of them are located in mesopore range. The textural data of these samples are listed in Table 1. We can find that the BET specific surface area of TiO₂-A, TiO₂-B, and TiO₂-R is 70.8, 57.6, and 28.9 m² g⁻¹, respectively. With the loading of CeO₂ on the surface of these TiO₂ supports, the BET specific surface area decreases to 59.6, 53.0, and 25.7 m² g⁻¹, respectively. Furthermore, the total pore volume of TiO₂-A and TiO₂-B decreases obviously after the introduction of CeO₂, which indicates that CeO₂ is mainly located at the bottom of mesopores. However, the total pore volume of TiO₂-R has no obvious change before and after the loading of CeO₂, suggesting that CeO₂ mainly locates on the outer surface of TiO₂-R.

3.2. Reduction behavior (H₂-TPR)

H₂-TPR is used to investigate the reduction properties of these supported ceria-based catalysts, as shown in Fig. 4. Moreover, the results of TiO₂-A, TiO₂-B, and TiO₂-R supports, as well as pure CeO₂ are also given in this figure for comparison. It can be seen from Fig. 4(a) that TiO₂-A, TiO₂-B, and TiO₂-R supports exhibit the reduction peak at 571, 677, and 551 °C, respectively. Pure CeO₂ presents two reduction peaks around 507 and 805 °C, which are assigned to the reduction of surface CeO₂ and bulk CeO₂, respectively [13,14]. In addition, H₂ consumption of TiO₂-A, TiO₂-B, TiO₂-R, and pure CeO₂ is 123, 243, 161, and 1960 μmol g⁻¹, which can be used for calculating the theoretical H₂ consumption of CeO₂/TiO₂-A, CeO₂/TiO₂-B, and CeO₂/TiO₂-R catalysts. Interestingly, Fig. 4(b) shows that the H₂-TPR profiles of CeO₂/TiO₂-A, CeO₂/TiO₂-B, and CeO₂/TiO₂-R catalysts are very similar, all of which exhibit three reduction peaks between 300 and 900 °C, labeled as α, β, and γ, respectively. The low-temperature reduction peak (α) around 500 °C and the high-temperature reduction peak (γ) around 800 °C can be respectively attributed to the reduction of surface dispersed CeO₂ and clustered (bulk-like) CeO₂ [32–34]. And the mid-temperature reduction peak (β) around 650 °C may be ascribed to the reduction of Ce-O-Ti species, which generates from the interaction between CeO₂ and TiO₂. Furthermore, the reduction peak temperature and H₂ consumption of these supported ceria-based catalysts are summarized in Table 2. Interestingly, the actual H₂ consumption of CeO₂/TiO₂-A, CeO₂/TiO₂-B, and CeO₂/TiO₂-R catalysts is obviously larger than the corresponding theoretical H₂ consumption (shown in the parentheses in Table 2). This phenomenon further confirms that some interaction exists between these TiO₂ supports and the surface dispersed CeO₂, which can promote the reduction of each other efficiently. Moreover, we can find that the reduction peak temperature of CeO₂/TiO₂-R catalyst is obviously lower than that of CeO₂/TiO₂-A and CeO₂/TiO₂-B catalysts. H₂ consumption of these catalysts

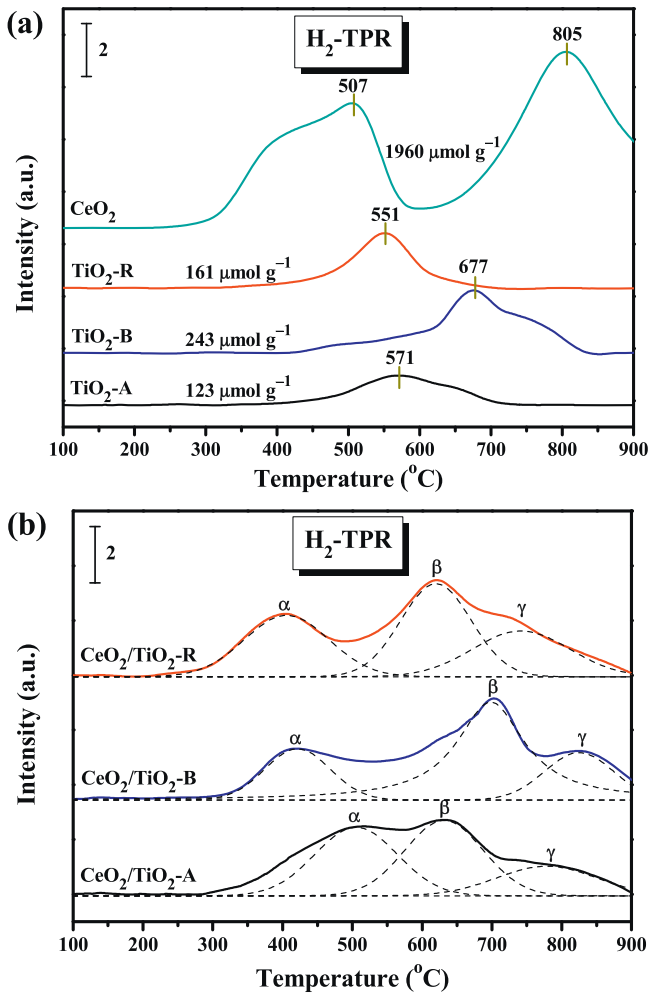


Fig. 4. H₂-TPR profiles of (a) these TiO₂ supports (and pure CeO₂), and (b) the corresponding supported ceria-based catalysts.

Table 2

Peak temperature and H₂ consumption of these supported ceria-based catalysts obtained from H₂-TPR.

Catalysts	Peak temperature (°C)			H ₂ consumption (μmol g ⁻¹)			
	T _α	T _β	T _γ	S _α	S _β	S _γ	S _α + S _β + S _γ
CeO ₂ /TiO ₂ -A	507	635	792	242	253	92	587 (241)
CeO ₂ /TiO ₂ -B	421	702	826	143	359	124	626 (354)
CeO ₂ /TiO ₂ -R	405	620	745	222	281	174	677 (277)

can be ranked by CeO₂/TiO₂-R > CeO₂/TiO₂-B > CeO₂/TiO₂-A. These phenomena indicate that the reduction property of CeO₂/TiO₂-R is the best among these catalysts due to the strongest interaction between CeO₂ and TiO₂-R, which is supported by the theoretical study results of Pan et al. [35]. They reported that the formation energy of Ti⁴⁺ defects is 11.76, 11.19, and 10.86 eV for anatase, brookite, and rutile TiO₂, respectively, obtained by theoretical calculation. The result suggests that the transfer of Ti⁴⁺ to generate Ti⁴⁺ defects in rutile TiO₂ is the easiest among these crystal forms of TiO₂. Therefore, it could be deduced that there is the strongest interaction between CeO₂ and TiO₂-R among these catalysts due to the easiest transfer of Ti⁴⁺ and the subsequent occupation of Ti⁴⁺ defects by Ce⁴⁺ through their interface in the preparation process of CeO₂/TiO₂-R catalyst.

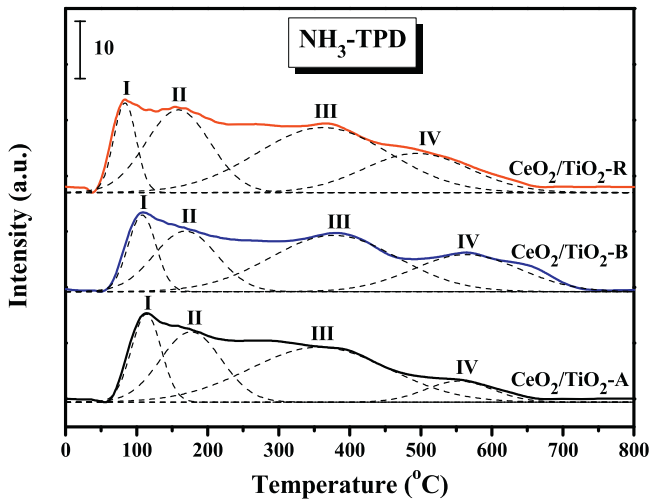


Fig. 5. NH₃-TPD profiles of these supported ceria-based catalysts.

Table 3

Quantitative analysis of NH₃-TPD over these supported ceria-based catalysts.

Catalysts	Acid amount (a.u.)				Total acid amount (a.u.)
	S _I	S _{II}	S _{III}	S _{IV}	
CeO ₂ /TiO ₂ -A	829	1357	2411	446	5043
CeO ₂ /TiO ₂ -B	676	1200	2253	1239	5368
CeO ₂ /TiO ₂ -R	634	1669	2715	1306	6324

3.3. Surface acid property (NH₃-TPD and NH₃-adsorption *in situ* DRIFTS)

Surface acidity of these supported ceria-based catalysts is measured by NH₃-TPD, and the corresponding results are presented in Fig. 5. It is widely reported that the position and area of the desorption peak are closely related to the strength and amount of surface acid sites over the catalysts, respectively [7,36]. We can see from Fig. 5 that NH₃-TPD profiles of CeO₂/TiO₂-A, CeO₂/TiO₂-B, and CeO₂/TiO₂-R catalysts are very similar, which exhibit four desorption peaks during the temperature range of measurement, labeled as I, II, III, and IV. These desorption peaks can be attributed to the desorption of physisorbed NH₃, and NH₃ species desorbed from weak acid sites, medium strength acid sites, and strong acid sites, respectively [7]. Because NH₄⁺ ions bonded on Brønsted (B) acid sites are less thermally stable than NH₃ molecules coordinated to Lewis (L) acid sites, it could be concluded that the desorption peaks at low temperature (below 300 °C) can be mainly attributed to NH₄⁺ ions bonded on B acid sites, while the desorption peaks at high temperature (above 300 °C) can be related to the desorption of NH₃ molecules from L acid sites [36]. This conclusion can be supported by the results of NH₃-adsorption *in situ* DRIFTS in Fig. 6. Quantitative analysis data of NH₃-TPD over these supported ceria-based catalysts are listed in Table 3. Interestingly, it can be seen from this table that the total acid amounts of these catalysts give a sequence of CeO₂/TiO₂-R > CeO₂/TiO₂-B > CeO₂/TiO₂-A. The largest total acid amount of CeO₂/TiO₂-R among these supported ceria-based catalysts may be related to the easiest formation of Ti⁴⁺ defects and the strongest interaction between CeO₂ and TiO₂-R over CeO₂/TiO₂-R catalyst, which is beneficial to the adsorption of NH₃ molecules.

Surface acidity of catalysts playing a key role in NH₃-SCR reaction has been recognized after decades of research. However, this is still controversial whether B acid or L acid is more important. NH₃-adsorption *in situ* DRIFTS technique is an efficient approach to distinguish B acid and L acid, which is carried out over these supported ceria-based catalysts, as shown in Fig. 6. For CeO₂/TiO₂-

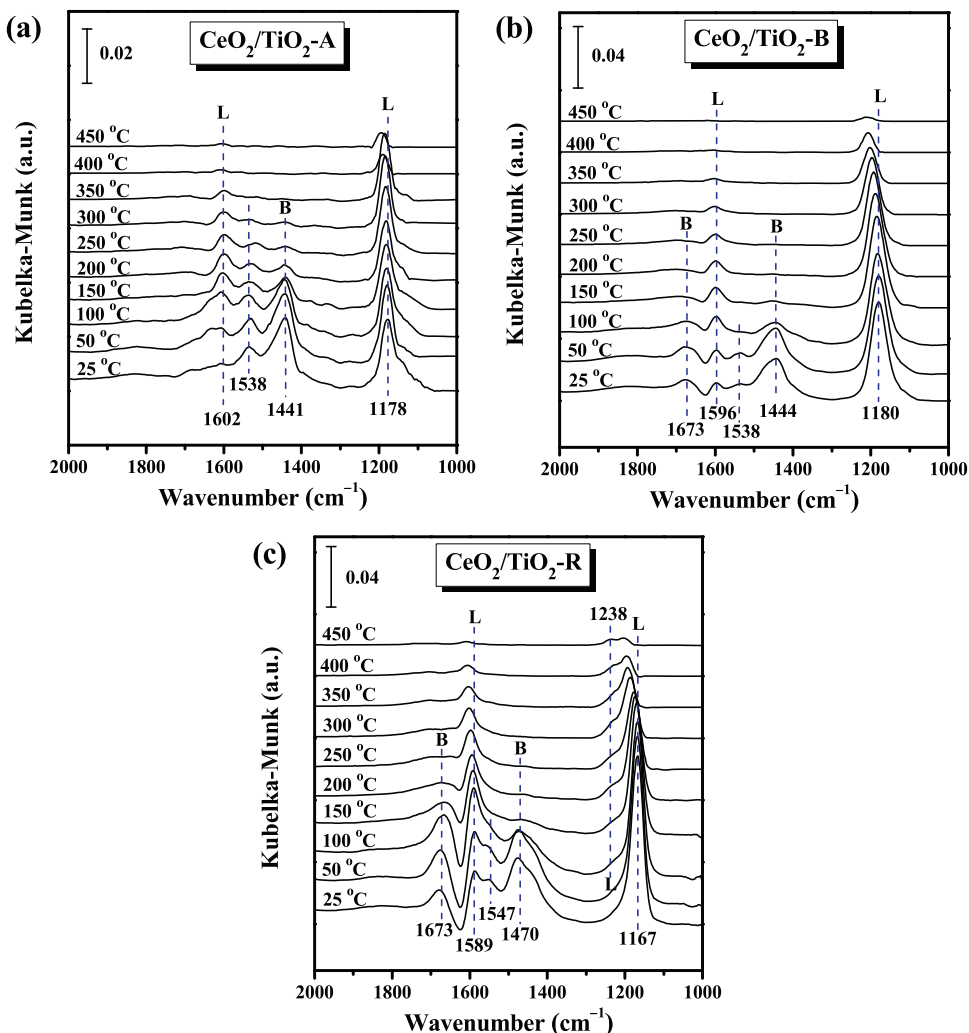


Fig. 6. NH_3 -adsorption *in situ* DRIFTS of these supported ceria-based catalysts: (a) $\text{CeO}_2/\text{TiO}_2\text{-A}$, (b) $\text{CeO}_2/\text{TiO}_2\text{-B}$, and (c) $\text{CeO}_2/\text{TiO}_2\text{-R}$.

A catalyst (Fig. 6(a)), when it is exposed to $\text{NH}_3\text{-N}_2$ mixed gases at room temperature (25°C), several IR bands are detected during the wavenumber range of $1000\text{--}2000\text{ cm}^{-1}$. According to the literatures [8,9,17,18], the bands at 1178 and 1602 cm^{-1} are attributed to NH_3 species coordinately adsorbed on L acid sites; while the band at 1441 cm^{-1} is ascribed to NH_4^+ ions bonded on B acid sites; interestingly, the weak band at 1538 cm^{-1} is related to the split ν_3 mode of bidentate nitrates, which result from the oxidation of the adsorbed NH_3 species by surface oxygen over $\text{CeO}_2/\text{TiO}_2\text{-A}$ catalyst. With the increase of temperature, all of these IR bands weaken obviously. Especially, the bands of B acid (1441 cm^{-1}) and bidentate nitrates (1538 cm^{-1}) disappear completely at 350°C due to the desorption or/and decomposition. However, the bands of L acid (1178 and 1602 cm^{-1}) are still existed even at 450°C owing to the strong adsorption for the coordinated NH_3 species. These phenomena are well consistent with the results of $\text{NH}_3\text{-TPD}$.

Similarly, with regard to $\text{CeO}_2/\text{TiO}_2\text{-B}$ and $\text{CeO}_2/\text{TiO}_2\text{-R}$ catalysts (Fig. 6(b) and (c)), the bands of L acid, B acid, and bidentate nitrates are also observed at the corresponding positions. Interestingly, a new band appears at 1673 cm^{-1} over $\text{CeO}_2/\text{TiO}_2\text{-B}$ and $\text{CeO}_2/\text{TiO}_2\text{-R}$ catalysts, which is also assigned to NH_4^+ ions fixed on B acid sites [8,17]. This band may be generated from the reaction of NH_3 species and the surface hydroxyl group (-OH) adsorbed on the defective sites of $\text{CeO}_2/\text{TiO}_2\text{-B}$ and $\text{CeO}_2/\text{TiO}_2\text{-R}$ catalysts. Furthermore, the band of bidentate nitrates over $\text{CeO}_2/\text{TiO}_2\text{-B}$ and $\text{CeO}_2/\text{TiO}_2\text{-R}$ catalysts disappears at a lower temperature of 150°C .

compared with $\text{CeO}_2/\text{TiO}_2\text{-A}$ catalyst, indicating the easier desorption or/and decomposition of bidentate nitrates, which is beneficial to the excellent catalytic performance for $\text{NH}_3\text{-SCR}$ reaction. Especially, with the temperature increases to 100°C , a new band can be detected at 1238 cm^{-1} over $\text{CeO}_2/\text{TiO}_2\text{-R}$ catalyst, which is attributed to NH_3 species coordinately adsorbed on L acid sites [8,9]. This band may be related to the easiest transfer of Ti^{4+} from the lattice of $\text{TiO}_2\text{-R}$ to the surface of $\text{CeO}_2/\text{TiO}_2\text{-R}$ catalyst, and then NH_3 species desorbed from the adjacent acid sites and adsorbed on the coordinately unsaturated Ti^{4+} centers, which is conducive to the adsorption and activation of NH_3 species, and further promotes the progress of $\text{NH}_3\text{-SCR}$ reaction. Moreover, Fig. 6 exhibits that the band intensity of L acid is remarkably stronger than that of B acid over these supported ceria-based catalysts, and L acid exists in the whole effective temperature range of $\text{NH}_3\text{-SCR}$ reaction, while B acid disappears at a lower temperature, which indicate that L acid is more important than B acid for $\text{NH}_3\text{-SCR}$ reaction in the present work.

3.4. Interaction with reactants ($\text{NO} + \text{NH}_3 + \text{O}_2$ co-adsorption *in situ* DRIFTS)

With the purpose of investigating the interaction between these supported ceria-based catalysts and reactants to further understand the $\text{NH}_3\text{-SCR}$ reaction mechanism, $\text{NO} + \text{NH}_3 + \text{O}_2$ co-adsorption *in situ* DRIFTS experiments were carried out. Firstly,

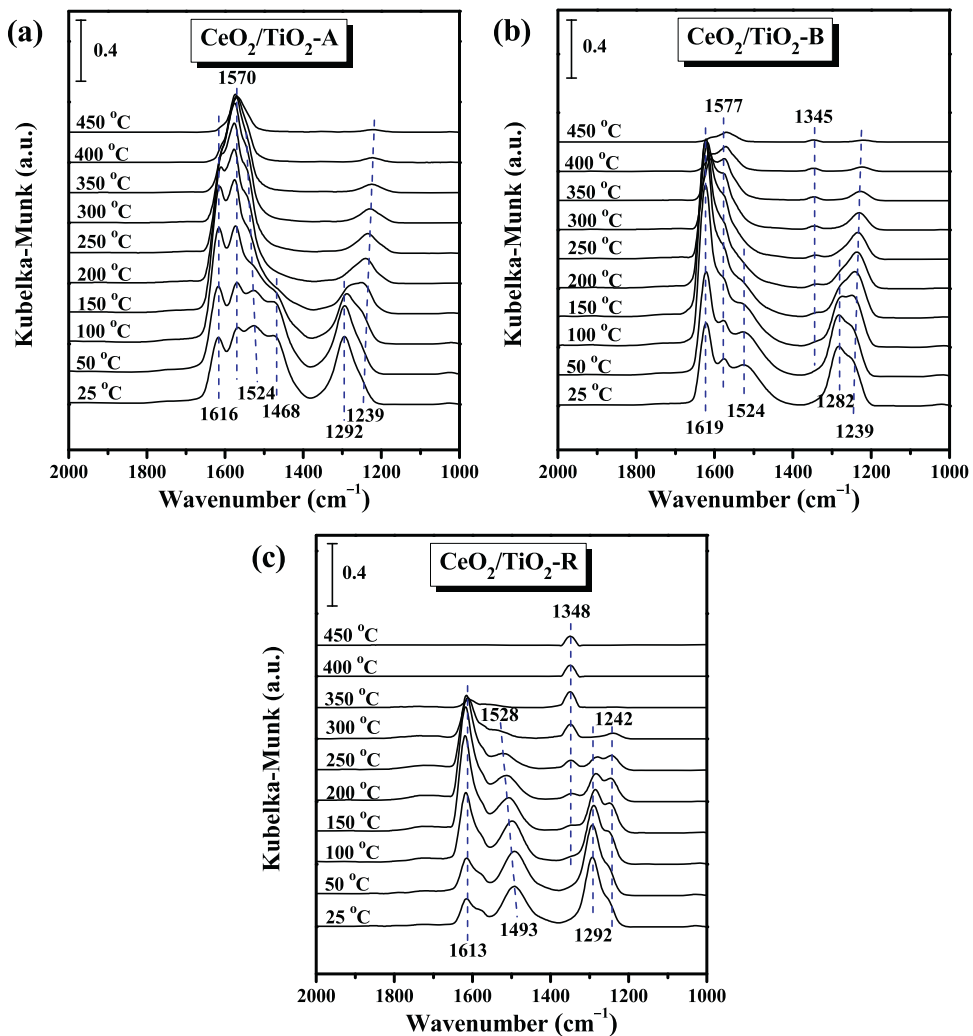


Fig. 7. NO + NH₃ + O₂ co-adsorption *in situ* DRIFTS of these supported ceria-based catalysts: (a) CeO₂/TiO₂-A, (b) CeO₂/TiO₂-B, and (c) CeO₂/TiO₂-R.

the catalyst was placed in an *in situ* DRIFTS cell and pretreated by high purified N₂ at 450 °C for 1 h to remove the physisorbed water. Secondly, the sample background of each target temperature was collected during the cooling process. At room temperature (25 °C), the sample was exposed to NO–NH₃–O₂–N₂ mixture (3000 ppm NO, 3000 ppm NH₃, and 5.0% O₂ by volume) at a rate of 50 ml min⁻¹ for 1 h to be saturated. Finally, *in situ* DRIFTS were recorded at various target temperatures from room temperature to 450 °C at a rate of 10 °C min⁻¹ by subtraction of the corresponding sample background. The NO + NH₃ + O₂ co-adsorption *in situ* DRIFTS results of these supported ceria-based catalysts are presented in Fig. 7. With regard to CeO₂/TiO₂-A catalyst (Fig. 7(a)), when it is exposed to NO–NH₃–O₂–N₂ mixed gases at room temperature (25 °C), several IR vibration bands are detected between 1000 and 2000 cm⁻¹. According to the literatures [9,13,37,38], the band at 1616 cm⁻¹ can be attributed to the bridging bidentate nitrates; the bands at 1570 and 1239 cm⁻¹ are assigned to the chelating bidentate nitrates; the band at 1524 cm⁻¹ is related to the split ν_3 mode of bidentate nitrates; while the bands at 1468 and 1292 cm⁻¹ can be ascribed to the monodentate nitrates. These results suggest that NO molecules can be also adsorbed on the surface of the supported ceria-based catalyst to generate nitrates. Unfortunately, the IR vibration band intensity of the adsorbed NO_x species is too strong, so that the IR signals of the adsorbed NH₃ species are covered. Some interesting phenomena can be found during the heating process, the

bands of monodentate nitrates (1468 and 1292 cm⁻¹) disappear at 200 °C due to the poor thermal stability; the band intensity of bridging bidentate nitrates (1616 cm⁻¹) and chelating bidentate nitrates (1570 and 1239 cm⁻¹) increases with the elevation of temperature firstly, and then decreases with the further increase of temperature, which is related to the reaction between the adsorbed NO_x and NH₃ species, as well as the transformation and dissociation of the adsorbed NO_x species. However, these bidentate nitrates don't disappear even at 450 °C owing to the strong adsorption.

Similarly, for CeO₂/TiO₂-B and CeO₂/TiO₂-R catalysts (Fig. 7(b) and (c)), the bands of bridging bidentate nitrates, chelating bidentate nitrates, split ν_3 mode of bidentate nitrates, and monodentate nitrates are also observed at the corresponding positions. Interestingly, when the temperature increases to 100 °C, a new band appears at 1345–1348 cm⁻¹ over CeO₂/TiO₂-B and CeO₂/TiO₂-R catalysts, which can be attributed to the intermediate species generated by the reaction of the adsorbed NO_x and NH₃ species [37]. This phenomenon suggests that the catalytic performance of CeO₂/TiO₂-B and CeO₂/TiO₂-R catalysts maybe better than that of CeO₂/TiO₂-A catalyst for NH₃-SCR reaction. Furthermore, with regard to CeO₂/TiO₂-R catalyst, all of the bridging bidentate nitrates, chelating bidentate nitrates, split ν_3 mode of bidentate nitrates, and monodentate nitrates disappear completely at 400 °C. The reason maybe that the strongest interaction between CeO₂ and TiO₂-R over CeO₂/TiO₂-R catalyst and its best reduction property

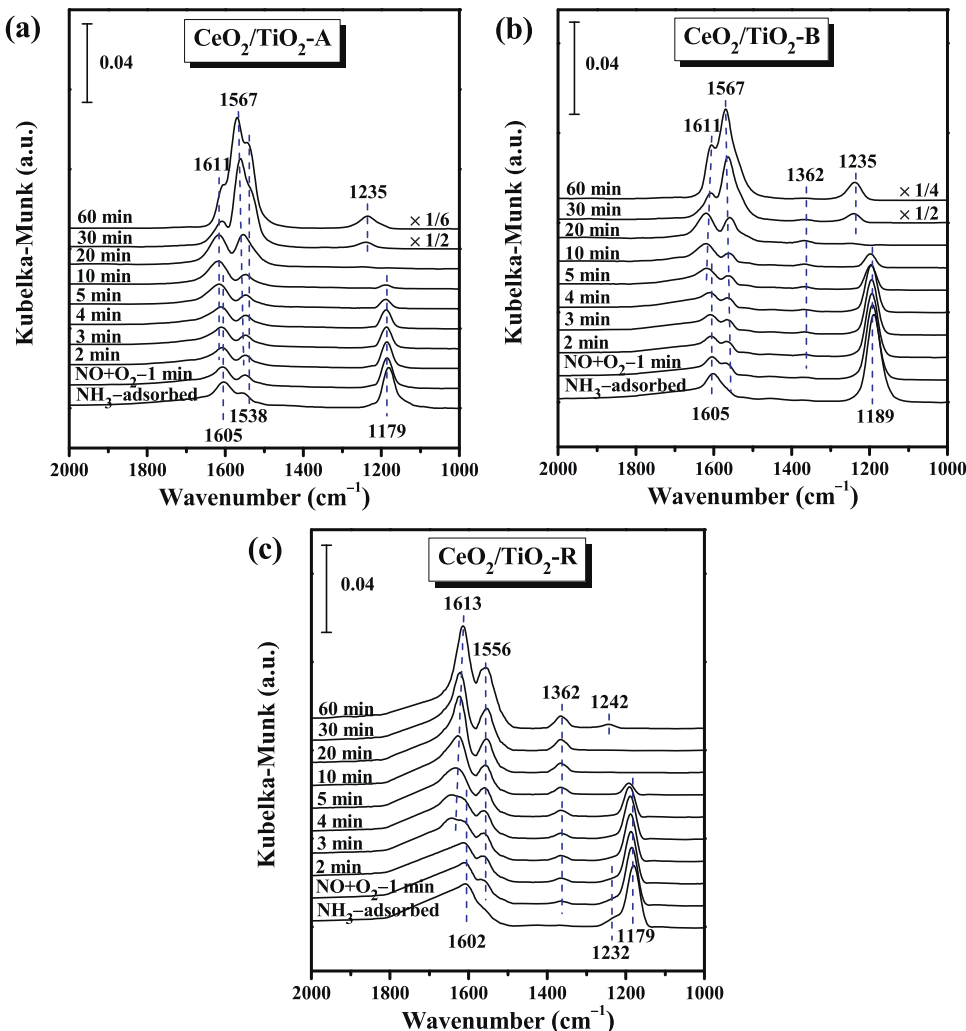


Fig. 8. Time-resolved $\text{NO} + \text{O}_2$ adsorption *in situ* DRIFTS of these supported ceria-based catalysts pre-adsorbed NH_3 at 300°C : (a) $\text{CeO}_2/\text{TiO}_2\text{-A}$, (b) $\text{CeO}_2/\text{TiO}_2\text{-B}$, and (c) $\text{CeO}_2/\text{TiO}_2\text{-R}$.

cause the back-donation of electrons to the anti-bonding orbit of NO_x species, which can weaken the N–O bond, and further promote the reaction of the adsorbed NO_x and NH_3 species, as well as the transformation and dissociation of the adsorbed NO_x species, and consequently result in excellent catalytic performance.

Indeed, the IR vibration band intensity of the adsorbed NO_x species over these supported ceria-based catalysts is too strong, which leads to that the IR signals of the adsorbed NH_3 species are covered. Therefore, in order to investigate the reaction between the adsorbed NH_3 and NO_x species intuitively, time-resolved $\text{NO} + \text{O}_2$ adsorption *in situ* DRIFTS of these supported ceria-based catalysts pre-adsorbed NH_3 at 300°C were carried out, and the corresponding results are displayed in Fig. 8. It can be seen from Fig. 8(a) that when $\text{CeO}_2/\text{TiO}_2\text{-A}$ catalyst is saturated by NH_3 at 300°C , the bands of L acid (1605 and 1179 cm^{-1}) and split ν_3 mode of bidentate nitrates (1538 cm^{-1}) can be detected. Then, NH_3 gas is cut off, and $\text{NO} + \text{O}_2$ gas is switched on. We can find that the band intensity of L acid (1605 and 1179 cm^{-1}) weakens obviously with the increase of $\text{NO} + \text{O}_2$ injection time, and disappears completely at 20 min . However, with the increase of $\text{NO} + \text{O}_2$ injection time, the band intensity of split ν_3 mode of bidentate nitrates (1538 cm^{-1}) strengthens remarkably, and some new IR signals of bridging bidentate nitrates (1611 cm^{-1}) and chelating bidentate nitrates (1567 and 1235 cm^{-1}) can be observed. These phenomena suggest that

the adsorbed NH_3 species can react with the adsorbed NO_x species efficiently.

Furthermore, only L acid can be detected over $\text{CeO}_2/\text{TiO}_2\text{-B}$ and $\text{CeO}_2/\text{TiO}_2\text{-R}$ catalysts (Fig. 8(b) and (c)) when they are saturated by NH_3 at 300°C . The change trend of L acid, bridging bidentate nitrates, and chelating bidentate nitrates with the increase of $\text{NO} + \text{O}_2$ injection time over $\text{CeO}_2/\text{TiO}_2\text{-B}$ and $\text{CeO}_2/\text{TiO}_2\text{-R}$ catalysts is similar to that of $\text{CeO}_2/\text{TiO}_2\text{-A}$ catalyst. However, an intermediate species generated by the reaction of the adsorbed NO_x and NH_3 species can be detected at 1362 cm^{-1} over $\text{CeO}_2/\text{TiO}_2\text{-B}$ and $\text{CeO}_2/\text{TiO}_2\text{-R}$ catalysts when $\text{NO} + \text{O}_2$ is introduced, which suggests that the catalytic performance of $\text{CeO}_2/\text{TiO}_2\text{-B}$ and $\text{CeO}_2/\text{TiO}_2\text{-R}$ catalysts maybe better than that of $\text{CeO}_2/\text{TiO}_2\text{-A}$ catalyst for $\text{NH}_3\text{-SCR}$ reaction. Moreover, we find that only L acid can be detected over these supported ceria-based catalysts when they are saturated by NH_3 at 300°C , while B acid is absent. However, all of these supported ceria-based catalysts exhibit high catalytic activity (above 80%) for $\text{NH}_3\text{-SCR}$ reaction at 300°C (see Fig. 10). These phenomena suggest that L acid is more important than B acid for $\text{NH}_3\text{-SCR}$ reaction in the present work.

3.5. Surface analysis (XPS)

It is well known that surface composition and oxidation states of catalysts are very important for $\text{NH}_3\text{-SCR}$ reaction, which can

Table 4

Surface composition and atomic ratio of these supported ceria-based catalysts calculated from XPS.

Catalysts	Atomic concentration (at.%)			Atomic ratio (%)		
	Ce	Ti	O	Ce/(Ce + Ti)	Ce ³⁺ /(Ce ³⁺ + Ce ⁴⁺)	O''/(O'' + O')
CeO ₂ /TiO ₂ -A	1.22	26.53	72.25	4.40	27.15	25.80
CeO ₂ /TiO ₂ -B	1.71	26.85	71.44	5.99	33.37	27.97
CeO ₂ /TiO ₂ -R	2.26	26.62	71.12	7.83	35.29	28.43

remarkably influence the adsorption and activation of reactant molecules. Therefore, the surface properties of these supported ceria-based catalysts are investigated by XPS, and the corresponding results are displayed in Fig. 9. It can be seen from Fig. 9(a) that the complex Ce 3d spectra of CeO₂/TiO₂-A, CeO₂/TiO₂-B, and CeO₂/TiO₂-R catalysts are fitted with eight binding energy peaks, labeled as u'', u', u⁰(u), and v'', v', v⁰(v), respectively. According to the literatures [11,20,32,39–41], u' and v' are attributed to surface Ce³⁺ species, while the other six binding energy peaks are ascribed to the full oxidation state Ce⁴⁺, which indicate that both of Ce³⁺ and Ce⁴⁺ species co-exist on the surface of these supported ceria-based catalysts. The appearance of surface Ce³⁺ species is bound to result in the formation of oxygen vacancy, which is beneficial to the dissociation of NO molecules, and further promotes the enhancement of catalytic performance for NH₃-SCR reaction. Therefore, the content of surface Ce³⁺ over these supported ceria-based catalysts is calculated by the following equation [42,43], and listed in Table 4.

$$\text{Ce}^{3+} (\%) = \frac{S_u + S_v}{\Sigma (S_u + S_v)} \times 100$$

Table 4 exhibits that the content of surface Ce³⁺ over these supported ceria-based catalysts is in the order of CeO₂/TiO₂-R > CeO₂/TiO₂-B > CeO₂/TiO₂-A, which may be related to the interaction between CeO₂ and TiO₂, as well as the dispersion of CeO₂ on the surface of TiO₂. It is widely reported that there is some strong interaction between CeO₂ and TiO₂ over CeO₂/TiO₂ catalysts through the transfer of electrons [13–15,37]. However, anatase, brookite, and rutile TiO₂ have different surface atomic arrangement structures, which can influence the difficulty degree of electron transfer, and further lead to different content of surface Ce³⁺. Furthermore, it can be seen from Table 4 that the value of Ce/(Ce + Ti) is ranked by CeO₂/TiO₂-R > CeO₂/TiO₂-B > CeO₂/TiO₂-A, which indicates that the dispersion of CeO₂ on the surface of TiO₂-R is the best, while on the surface of TiO₂-A is the worst. Some researchers reported that the content of surface Ce³⁺ in the particles increases with the decrease of crystallite size [44,45], which suggests that the dispersion of CeO₂ on the surface of TiO₂ can also affect the surface Ce³⁺ content of these supported ceria-based catalysts.

Fig. 9(b) presents Ti 2p spectra of these supported ceria-based catalysts. The binding energy peak of Ti 2p_{3/2} can be observed at 458.2, 458.0, and 458.0 eV over CeO₂/TiO₂-A, CeO₂/TiO₂-B, and CeO₂/TiO₂-R catalysts, respectively, which is slightly lower than that of Ti⁴⁺ (458.4 eV) in pure TiO₂ [13,46]. This phenomenon suggests that a small amount of Ti³⁺ may exist accompanied by Ti⁴⁺ on the surface of these supported ceria-based catalysts due to the interaction between CeO₂ and TiO₂ through Ce-O-Ti bridge bonds (*i.e.*, the electron transfer of Ce³⁺ + Ti⁴⁺ ⇌ Ce⁴⁺ + Ti³⁺ shifts to right). Furthermore, we can find that Ti 2p_{3/2} binding energy peak of CeO₂/TiO₂-B and CeO₂/TiO₂-R catalysts is lower than that of CeO₂/TiO₂-A catalyst, which indicates that the electron transfer between Ce and Ti ions in CeO₂/TiO₂-B and CeO₂/TiO₂-R catalysts is easier than that in CeO₂/TiO₂-A catalyst. It seems to contradictory with the order of surface Ce³⁺ content (CeO₂/TiO₂-R > CeO₂/TiO₂-B > CeO₂/TiO₂-A). In actual fact, this unusual phenomenon can be interpreted by

the formation of surface oxygen vacancy to maintain the charge balance.

O 1s spectra of these supported ceria-based catalysts are fitted with two components, as shown in Fig. 9(c). All of them exhibit a strong binding energy peak at 529.3 eV and a shoulder around 530.9 eV, labeled as O' and O'', which can be attributed to the lattice oxygen, and surface adsorbed oxygen species fixed on defective sites (such as oxygen vacancy), respectively [9,13,17]. It is well known that the surface adsorbed oxygen species is beneficial to the oxidation of NO to NO₂, and further promotes the progress of NH₃-SCR reaction through a “fast SCR” route [9]. Therefore, the content of surface adsorbed oxygen species (expressed as O''/(O'' + O')) over these supported ceria-based catalysts is calculated and listed in Table 4. It can be seen from this table that the value of O''/(O'' + O') is ranked by CeO₂/TiO₂-R > CeO₂/TiO₂-B > CeO₂/TiO₂-A, which is consistent with the order of surface Ce³⁺ content.

3.6. Catalytic performance and H₂O + SO₂ resistance (NH₃-SCR model reaction)

The catalytic performance of these TiO₂ supports and the corresponding supported ceria-based catalysts is evaluated by NH₃-SCR model reaction, and the corresponding results are given in Fig. 10. It can be seen from Fig. 10(a) that NO_x conversion of these samples is strongly dependent on the reaction temperature. With regard to these TiO₂ supports, they exhibit poor reactivity below 300 °C. However, the reactivity of these TiO₂ supports increases obviously when the reaction temperature is higher than 300 °C, and gives a sequence of TiO₂-R > TiO₂-B > TiO₂-A, which may be related to the different surface atomic arrangement structures and the formation difficulty degree of defective sites over these TiO₂ supports. In addition, we can find that NO_x conversion of these supported ceria-based catalysts is remarkably higher than that of TiO₂-A, TiO₂-B, and TiO₂-R supports due to the interaction between CeO₂ and TiO₂ through the formation of Ce-O-Ti species. The reactivity of these supported ceria-based catalysts can be ranked by CeO₂/TiO₂-R > CeO₂/TiO₂-B > CeO₂/TiO₂-A, which is consistent with the order of reduction property, acid amount, surface Ce³⁺ content, and surface adsorbed oxygen species. Furthermore, all of these supported ceria-based catalysts present similar volcano-type reactivity curves, *i.e.*, the reactivity increases with the elevation of reaction temperature firstly, and then declines with further increase of reaction temperature due to the non-selective oxidation of reductant NH₃ molecules. Especially, CeO₂/TiO₂-R catalyst exhibits high NO_x conversion (above 80%) during a wide operating temperature window of 200–400 °C due to the most excellent reduction property as well as the largest amounts of acid sites, surface Ce³⁺ content, and surface adsorbed oxygen species among these supported ceria-based catalysts, which result from the strongest interaction between CeO₂ and TiO₂-R. The most excellent reduction property and the largest amount of surface adsorbed oxygen species are beneficial to the oxidation of NO to NO₂, which can promote the progress of NH₃-SCR reaction through a “fast SCR” route. On the other hand, the formation of oxygen vacancy accompanied by surface Ce³⁺ and the consumption of surface oxygen species is conducive to the dissociation of NO molecules. Moreover, the largest amount of acid sites can promote the adsorption and activation of

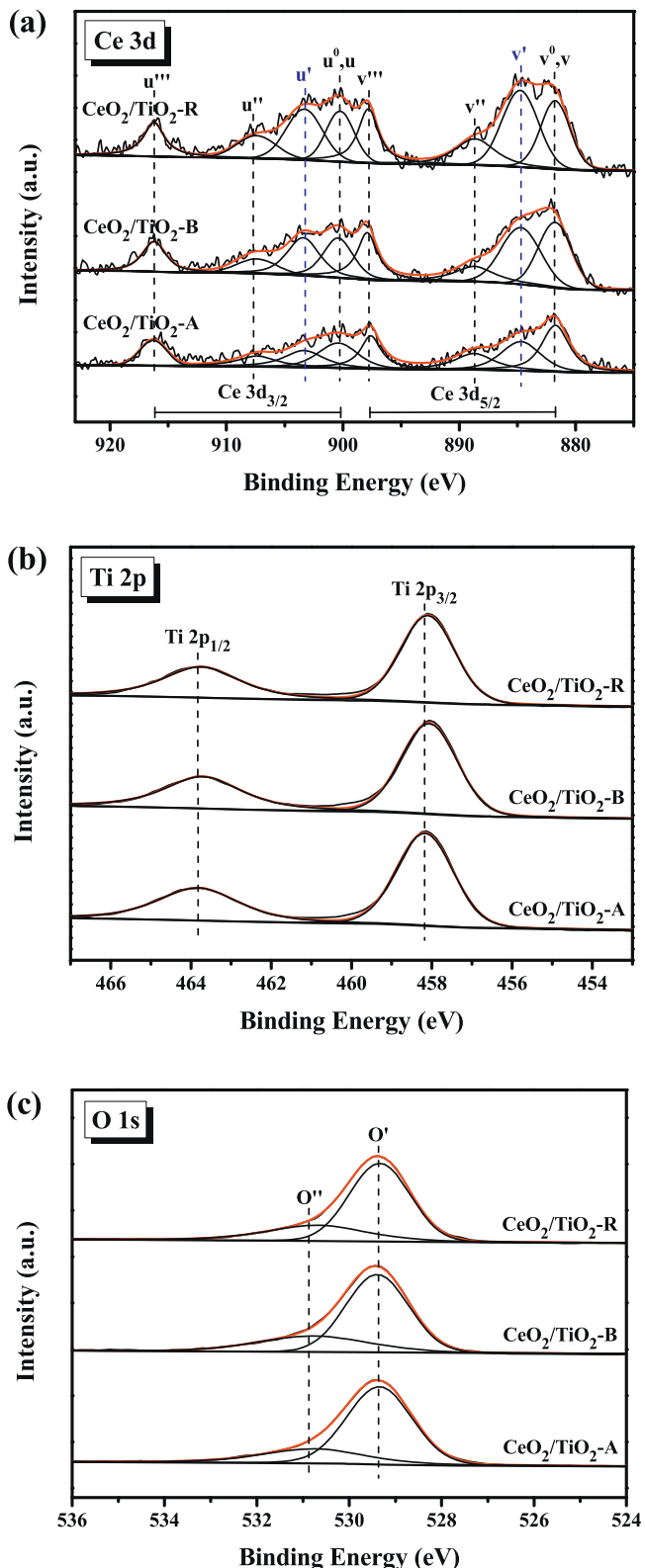
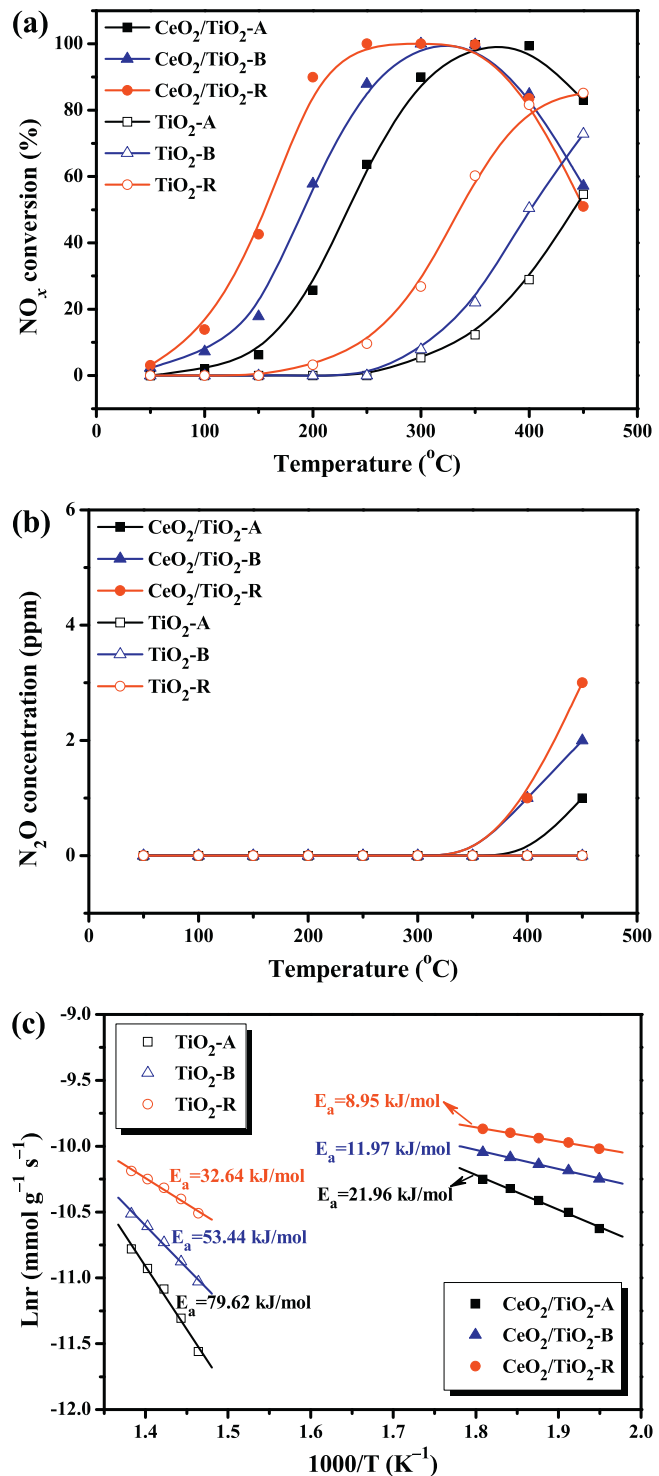


Fig. 9. XPS results of these supported ceria-based catalysts: (a) Ce 3d, (b) Ti 2p, and (c) O 1s.

NH₃ species, efficiently. All of these are beneficial to the enhancement of catalytic performance for NH₃-SCR reaction.

Furthermore, N₂O is a main by-product of NH₃-SCR reaction, which usually generates from the non-selective oxidation of NH₃ and partial reduction of NO_x, and can also cause serious



atmospheric pollution [47,48]. So, the generated N₂O concentration attracts more attention in NH₃-SCR reaction. In the present work, the generated N₂O concentration over these TiO₂ supports and the corresponding supported ceria-based catalysts was detected during the whole reaction temperature range (50–450 °C), and the corresponding results are exhibited in Fig. 10(b). We can find that N₂O concentration of these samples is very small (*i.e.*, not higher than 3 ppm) in the temperature range of 50–450 °C, which can be

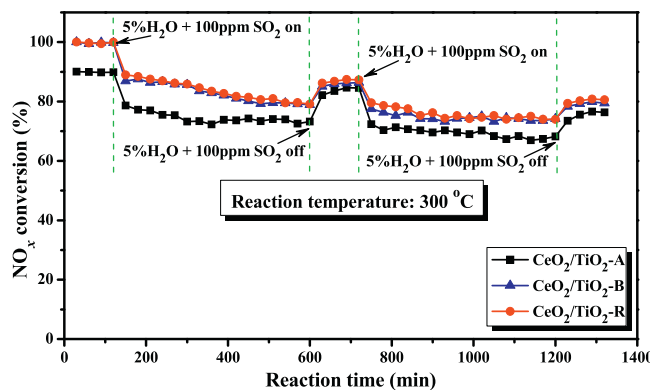


Fig. 11. Water and sulfur resistance of these supported ceria-based catalysts at 300 °C.

ignored. This phenomenon suggests that these samples have high selectivity for the catalytic reduction of NO_x to N_2 .

With the purpose of further understanding the difference of catalytic performance among these TiO_2 supports and the corresponding supported ceria-based catalysts, the apparent activation energy (E_a) of $\text{NH}_3\text{-SCR}$ reaction over these samples is investigated according to Arrhenius equation, as shown in Fig. 10(c). It is widely reported that $\text{NH}_3\text{-SCR}$ reaction over ceria-based catalysts is approximately first-order for NO_x and zero-order for NH_3 [12,49]. Therefore, E_a can be determined by the slope of Arrhenius plots with lower NO_x conversion (below 30%, in order to exclude the influence of diffusion) based on pseudo first-order reaction kinetic equation. Fig. 10(c) exhibits that the value of E_a over these supported ceria-based catalysts is in the order of $\text{CeO}_2/\text{TiO}_2\text{-A}$ ($21.96 \text{ kJ mol}^{-1}$) > $\text{CeO}_2/\text{TiO}_2\text{-B}$ ($11.97 \text{ kJ mol}^{-1}$) > $\text{CeO}_2/\text{TiO}_2\text{-R}$ (8.95 kJ mol^{-1}), which is owing to the different surface atomic arrangement structures of $\text{TiO}_2\text{-A}$, $\text{TiO}_2\text{-B}$, and $\text{TiO}_2\text{-R}$, as well as the different interaction between CeO_2 and TiO_2 (anatase, brookite, and rutile). This observation indicates that $\text{NH}_3\text{-SCR}$ reaction over these supported ceria-based catalysts follows different reaction routes, and the occurrence over $\text{CeO}_2/\text{TiO}_2\text{-R}$ catalyst is the easiest, which is in well agreement with the results of NO_x conversion. Moreover, the value of E_a over these supported ceria-based catalysts is obviously smaller than that of $\text{TiO}_2\text{-A}$ ($79.62 \text{ kJ mol}^{-1}$), $\text{TiO}_2\text{-B}$ ($53.44 \text{ kJ mol}^{-1}$), and $\text{TiO}_2\text{-R}$ ($32.64 \text{ kJ mol}^{-1}$) supports, which suggests that the loading of CeO_2 can efficiently decrease the energy barrier of $\text{NH}_3\text{-SCR}$ reaction.

The existence of H_2O and SO_2 is unavoidable in the practical application of denitrification catalysts. Therefore, the water and sulfur resistance of these supported ceria-based catalysts are explored for $\text{NH}_3\text{-SCR}$ reaction, and the reaction temperature is fixed at 300 °C, the corresponding results are displayed in Fig. 11. We can find that NO_x conversion of $\text{CeO}_2/\text{TiO}_2\text{-A}$, $\text{CeO}_2/\text{TiO}_2\text{-B}$, and $\text{CeO}_2/\text{TiO}_2\text{-R}$ catalysts is very stable in the absence of H_2O and SO_2 . However, it declines to some extent when H_2O (5%) and SO_2 (100 ppm) are introduced. Interestingly, NO_x conversion can be partially recovered after cutting off the injection of H_2O and SO_2 . Moreover, the catalytic activity of these supported ceria-based catalysts further decreases when H_2O and SO_2 are injected repeatedly, while it can be also partially recovered with the removal of H_2O and SO_2 . These phenomena indicate that H_2O and SO_2 can result in the reversible and irreversible deactivation of $\text{CeO}_2/\text{TiO}_2\text{-A}$, $\text{CeO}_2/\text{TiO}_2\text{-B}$, and $\text{CeO}_2/\text{TiO}_2\text{-R}$ catalysts, which may be related to the competitive adsorption of H_2O and NH_3 , the deposition of $(\text{NH}_4)_2\text{SO}_4$ and NH_4HSO_4 , as well as the sulfation of active components [10,17,50]. Furthermore, Fig. 11 shows that NO_x conversion of $\text{CeO}_2/\text{TiO}_2\text{-B}$ and $\text{CeO}_2/\text{TiO}_2\text{-R}$ catalysts is higher than that of $\text{CeO}_2/\text{TiO}_2\text{-A}$ catalyst in the presence of H_2O and SO_2 , but the decrease of NO_x conversion

over $\text{CeO}_2/\text{TiO}_2\text{-A}$ catalyst caused by H_2O and SO_2 poisoning is the most slight among these supported ceria-based catalysts, which suggests that the tolerance of H_2O and SO_2 over $\text{CeO}_2/\text{TiO}_2\text{-B}$ and $\text{CeO}_2/\text{TiO}_2\text{-R}$ catalysts still needs to be further enhanced.

4. Conclusions

In summary, a comparative study of $\text{CeO}_2/\text{TiO}_2\text{-A}$, $\text{CeO}_2/\text{TiO}_2\text{-B}$, and $\text{CeO}_2/\text{TiO}_2\text{-R}$ catalysts is carried out with the purpose of clarifying the influence of TiO_2 supports with different crystal forms on the physicochemical properties and catalytic performance of these supported ceria-based catalysts for $\text{NH}_3\text{-SCR}$ reaction. The obtained results indicate that CeO_2 species is highly dispersed on the surface of $\text{TiO}_2\text{-A}$, $\text{TiO}_2\text{-B}$, and $\text{TiO}_2\text{-R}$ supports, and strongly interacts with these TiO_2 supports. However, because of the different surface atomic arrangement structures of $\text{TiO}_2\text{-A}$, $\text{TiO}_2\text{-B}$, and $\text{TiO}_2\text{-R}$ supports, the interaction between CeO_2 and TiO_2 depends on the crystal form of TiO_2 , which leads to that the reduction property, acid amount, surface Ce^{3+} content, surface adsorbed oxygen species, and catalytic performance of these supported ceria-based catalysts are different from each other. Furthermore, $\text{CeO}_2/\text{TiO}_2\text{-R}$ catalyst exhibits the best physicochemical property and optimal catalytic performance for $\text{NH}_3\text{-SCR}$ reaction, but its tolerance of H_2O and SO_2 still needs to be further improved. Therefore, we will focus on the enhancement of water and sulfur resistance of $\text{CeO}_2/\text{TiO}_2\text{-R}$ catalyst in the near future.

Acknowledgements

The financial supports of the National Natural Science Foundation of China (21507130), the Chongqing Science & Technology Commission (cstc2016jcyjA0070, cstc2014pt-gc20002, cstc2014yykfC20003, cstckjcxljrc13), the Open Project Program of Jiangsu Key Laboratory of Vehicle Emissions Control (OVEC001, OVEC007), and the Open Project Program of Chongqing Key Laboratory of Catalysis and Functional Organic Molecules from Chongqing Technology and Business University (1456029) are gratefully acknowledged. Furthermore, we also thank Dr. Shuhan Yu in Nanjing University for XPS measurement.

References

- [1] G. Busca, L. Lietti, G. Ramis, F. Berti, Appl. Catal. B: Environ. 18 (1998) 1–36.
- [2] F. Giraud, J. Couble, C. Geantet, N. Guilhame, E. Puzenat, S. Gros, L. Porcheron, M. Kanniche, D. Bianchi, J. Phys. Chem. C 119 (2015) 16089–16105.
- [3] X.H. Xie, J.D. Lu, E. Hums, Q.X. Huang, Z.M. Lu, Energy Fuels 29 (2015) 3890–3896.
- [4] X. Zhao, L. Huang, H.R. Li, H. Hu, J. Han, L.Y. Shi, D.S. Zhang, Chin. J. Catal. 36 (2015) 1886–1899.
- [5] S.C. Xiong, X. Xiao, Y. Liao, H. Dang, W.P. Shan, S.J. Yang, Ind. Eng. Chem. Res. 54 (2015) 11011–11123.
- [6] N.Y. Topsøe, Science 265 (1994) 1217–1219.
- [7] K.A. Michalow-Mauke, Y. Lu, K. Kowalski, T. Graule, M. Nachtegaal, O. Kröcher, D. Ferri, ACS Catal. 5 (2015) 5657–5672.
- [8] S.P. Ding, F.D. Liu, X.Y. Shi, K. Liu, Z.H. Lian, L.J. Xie, H. He, ACS Appl. Mater. Interf. 7 (2015) 9497–9506.
- [9] J. Liu, X.Y. Li, Q.D. Zhao, J. Ke, H.N. Xiao, X.J. Lv, S.M. Liu, M. Tadé, S.B. Wang, Appl. Catal. B: Environ. 200 (2017) 297–308.
- [10] C.X. Liu, L. Chen, J.H. Li, L. Ma, H. Arandiyani, Y. Du, J.Y. Xu, J.M. Hao, Environ. Sci. Technol. 46 (2012) 6182–6189.
- [11] Z.M. Liu, Y.X. Liu, B.H. Chen, T.L. Zhu, L.L. Ma, Catal. Sci. Technol. 6 (2016) 6688–6696.
- [12] Y. Geng, W.P. Shan, S.C. Xiong, Y. Liao, S.J. Yang, F.D. Liu, Catal. Sci. Technol. 6 (2016) 3149–3155.
- [13] X.J. Yao, L. Zhang, L.L. Li, L.C. Liu, Y. Cao, X. Dong, F. Gao, Y. Deng, C.J. Tang, Z. Chen, L. Dong, Y. Chen, Appl. Catal. B: Environ. 150–151 (2014) 315–329.
- [14] P. Li, Y. Xin, Q. Li, Z.P. Wang, Z.L. Zhang, L.R. Zheng, Environ. Sci. Technol. 46 (2012) 9600–9605.
- [15] W.P. Shan, F.D. Liu, H. He, X.Y. Shi, C.B. Zhang, Catal. Today 184 (2012) 160–165.
- [16] Y. Peng, R.Y. Qu, X.Y. Zhang, J.H. Li, Chem. Commun. 49 (2013) 6215–6217.
- [17] L. Zhang, L.L. Li, Y. Cao, X.J. Yao, C.Y. Ge, F. Gao, Y. Deng, C.J. Tang, L. Dong, Appl. Catal. B: Environ. 165 (2015) 589–598.

- [18] H. Hu, S.X. Cai, H.R. Li, L. Huang, L.Y. Shi, D.S. Zhang, *ACS Catal.* 5 (2015) 6069–6077.
- [19] L.J. Zhang, S.P. Cui, H.X. Guo, X.Y. Ma, X.G. Luo, *Appl. Surf. Sci.* 355 (2015) 1116–1122.
- [20] T. Boningari, P.R. Ettireddy, A. Somogyvari, Y. Liu, A. Vorontsov, C.A. McDonald, P.G. Smirniotis, *J. Catal.* 325 (2015) 145–155.
- [21] J. Zhao, Y. Wang, Y.X. Li, X. Yue, C.Y. Wang, *Catal. Sci. Technol.* 6 (2016) 7967–7975.
- [22] Y.F. Li, A. Selloni, *ACS Catal.* 6 (2016) 4769–4774.
- [23] Q.L. Tay, X.H. Wang, X. Zhao, J.D. Hong, Q. Zhang, R. Xu, Z. Chen, *J. Catal.* 342 (2016) 55–62.
- [24] B.K. Mutuma, G.N. Shao, W.D. Kim, H.T. Kim, *J. Colloid Interf. Sci.* 442 (2015) 1–7.
- [25] Z.W. Yang, B. Wang, H. Cui, H. An, Y. Pan, J.P. Zhai, *J. Phys. Chem. C* 119 (2015) 16905–16912.
- [26] X.L. Wang, A. Kafizas, X.E. Li, S.J.A. Moniz, P.J.T. Reardon, J.W. Tang, I.P. Parkin, J.R. Durrant, *J. Phys. Chem. C* 119 (2015) 10439–10447.
- [27] R. Kaplan, B. Erjavec, G. Dražić, J. Grdadolnik, A. Pintar, *Appl. Catal. B: Environ.* 181 (2016) 465–474.
- [28] L.J. Liu, H.L. Zhao, J.M. Andino, Y. Li, *ACS Catal.* 2 (2012) 1817–1828.
- [29] M. Buchalska, M. Kobielsz, A. Matuszek, M. Pacia, S. Wojtyła, W. Macyk, *ACS Catal.* 5 (2015) 7424–7431.
- [30] H. Zhao, Y.M. Dong, P.P. Jiang, G.L. Wang, J.J. Zhang, *ACS Appl. Mater. Interf.* 7 (2015) 6451–6461.
- [31] K.S.W. Sing, D.H. Everett, R.A.W. Haul, L. Moscou, R.A. Pierotti, J. Rouquerol, T. Siemieniewska, *Pure Appl. Chem.* 57 (1985) 603–619.
- [32] X. Xiao, S.C. Xiong, Y.J. Shi, W.P. Shan, S.J. Yang, *J. Phys. Chem. C* 120 (2016) 1066–1076.
- [33] S.M. Lee, H.H. Lee, S.C. Hong, *Appl. Catal. A: Gen.* 470 (2014) 189–198.
- [34] X. Gao, Y. Jiang, Y.C. Fu, Y. Zhong, Z.Y. Luo, K.F. Cen, *Catal. Commun.* 11 (2010) 465–469.
- [35] H. Pan, B.H. Gu, Z.Y. Zhang, *J. Chem. Theory Comput.* 5 (2009) 3074–3078.
- [36] C. Fang, D.S. Zhang, S.X. Cai, L. Zhang, L. Huang, H.R. Li, P. Maitarad, L.Y. Shi, R.H. Gao, J.P. Zhang, *Nanoscale* 5 (2013) 9199–9207.
- [37] Y. Xiong, C.J. Tang, X.J. Yao, L. Zhang, L.L. Li, X.B. Wang, Y. Deng, F. Gao, L. Dong, *Appl. Catal. A: Gen.* 495 (2015) 206–216.
- [38] K.I. Hadjiivanov, *Catal. Rev.* 42 (2000) 71–144.
- [39] T. Boningari, D.K. Pappas, P.R. Ettireddy, A. Kotrba, P.G. Smirniotis, *Ind. Eng. Chem. Res.* 54 (2015) 2261–2273.
- [40] X. Li, J.H. Li, Y. Peng, X.S. Li, K.Z. Li, J.M. Hao, *J. Phys. Chem. C* 120 (2016) 18005–18014.
- [41] J. Han, J. Meeprasert, P. Maitarad, S. Nammuangruk, L.Y. Shi, D.S. Zhang, *J. Phys. Chem. C* 120 (2016) 1523–1533.
- [42] M.S.P. Francisco, V.R. Mastelaro, P.A.P. Nascente, A.O. Florentino, *J. Phys. Chem. B* 105 (2001) 10515–10522.
- [43] X.J. Yao, F. Gao, Q. Yu, L. Qi, C.J. Tang, L. Dong, Y. Chen, *Catal. Sci. Technol.* 3 (2013) 1355–1366.
- [44] H.J. Wiesmann, A.R. Moodenbaugh, R.F. Klie, Y.M. Zhu, D.O. Welch, M. Sueyaga, L.J. Wu, *Phys. Rev. B* 69 (2004) 125415.
- [45] R.K. Hailstone, A.G. DiFrancesco, J.G. Leong, T.D. Allston, K.J. Reed, *J. Phys. Chem. C* 113 (2009) 15155–15159.
- [46] R. Siavash Moakhar, G.K.L. Goh, A. Dolati, M. Ghorbani, *Appl. Catal. B: Environ.* 201 (2017) 411–418.
- [47] L. Zhang, L.Y. Shi, L. Huang, J.P. Zhang, R.H. Gao, D.S. Zhang, *ACS Catal.* 4 (2014) 1753–1763.
- [48] X.J. Yao, T.T. Kong, S.H. Yu, L.L. Li, F.M. Yang, L. Dong, *Appl. Surf. Sci.* 402 (2017) 208–217.
- [49] L.J. Yan, Y.Y. Liu, H. Hu, H.R. Li, L.Y. Shi, D.S. Zhang, *ChemCatChem* 8 (2016) 2267–2278.
- [50] J.H. Li, H.Z. Chang, L. Ma, J.M. Hao, R.T. Yang, *Catal. Today* 175 (2011) 147–156.